NAVAL POSTGRADUATE SCHOOL

MONTEREY, CALIFORNIA

THESIS

COMPENSATION OF TARGET IMAGE ABERRATIONS FOR MILITARY SYSTEMS USING MACHINE LEARNING

by

John C. Gale

June 2022

Thesis Advisor: Jae Jun Kim
Co-Advisor: Brij N. Agrawal

THIS PAGE INTENTIONALLY LEFT BLANK

REPORT DOCUMENTATION PAGE			*Form Approved OMB No. 0704-0188*

1. AGENCY USE ONLY *(Leave blank)*	**2. REPORT DATE** June 2022	**3. REPORT TYPE AND DATES COVERED** Master's thesis

4. TITLE AND SUBTITLE COMPENSATION OF TARGET IMAGE ABERRATIONS FOR MILITARY SYSTEMS USING MACHINE LEARNING	**5. FUNDING NUMBERS**
6. AUTHOR(S) John C. Gale	
7. PERFORMING ORGANIZATION NAME(S) AND ADDRESS(ES) Naval Postgraduate School Monterey, CA 93943-5000	**8. PERFORMING ORGANIZATION REPORT NUMBER**
9. SPONSORING / MONITORING AGENCY NAME(S) AND ADDRESS(ES) N/A	**10. SPONSORING / MONITORING AGENCY REPORT NUMBER**

11. SUPPLEMENTARY NOTES The views expressed in this thesis are those of the author and do not reflect the official policy or position of the Department of Defense or the U.S. Government.

12a. DISTRIBUTION / AVAILABILITY STATEMENT Approved for public release. Distribution is unlimited.	**12b. DISTRIBUTION CODE** A

13. ABSTRACT (maximum 200 words)

High energy laser (HEL) systems are susceptible to atmospheric turbulence when focusing on targets down range. Current HEL systems use wavefront sensors and complex adaptive optics systems to compensate for these aberrations. The primary objective of this thesis is to investigate target image aberration compensation techniques using machine learning algorithms, eliminating the need for complex wavefront sensing hardware. Target imagery will be obtained from the High Energy Laser Beam Control Research Testbed (HBCRT) and imagery aberrations will be simulated to provide necessary datasets for training and validation of the image aberration compensation methods. The performance of these techniques will be evaluated for military imaging applications.

14. SUBJECT TERMS machine learning, AI, deep learning, target imaging, high energy laser, HEL, High Energy Laser Beam Control Research Testbed, HBCRT	**15. NUMBER OF PAGES** 63
	16. PRICE CODE

17. SECURITY CLASSIFICATION OF REPORT Unclassified	**18. SECURITY CLASSIFICATION OF THIS PAGE** Unclassified	**19. SECURITY CLASSIFICATION OF ABSTRACT** Unclassified	**20. LIMITATION OF ABSTRACT** UU

NSN 7540-01-280-5500

Standard Form 298 (Rev. 2-89)
Prescribed by ANSI Std. 239-18

THIS PAGE INTENTIONALLY LEFT BLANK

Approved for public release. Distribution is unlimited.

COMPENSATION OF TARGET IMAGE ABERRATIONS FOR MILITARY SYSTEMS USING MACHINE LEARNING

John C. Gale
Ensign, United States Navy
BS, United States Naval Academy, 2021

Submitted in partial fulfillment of the
requirements for the degree of

MASTER OF SCIENCE IN ASTRONAUTICAL ENGINEERING

from the

NAVAL POSTGRADUATE SCHOOL
June 2022

Approved by: Jae Jun Kim
Advisor

Brij N. Agrawal
Co-Advisor

Garth V. Hobson
Chair, Department of Mechanical and Aerospace Engineering

THIS PAGE INTENTIONALLY LEFT BLANK

ABSTRACT

High energy laser (HEL) systems are susceptible to atmospheric turbulence when focusing on targets down range. Current HEL systems use wavefront sensors and complex adaptive optics systems to compensate for these aberrations. The primary objective of this thesis is to investigate target image aberration compensation techniques using machine learning algorithms, eliminating the need for complex wavefront sensing hardware. Target imagery will be obtained from the High Energy Laser Beam Control Research Testbed (HBCRT) and imagery aberrations will be simulated to provide necessary datasets for training and validation of the image aberration compensation methods. The performance of these techniques will be evaluated for military imaging applications.

THIS PAGE INTENTIONALLY LEFT BLANK

TABLE OF CONTENTS

LIST OF FIGURES

LIST OF TABLES

THIS PAGE INTENTIONALLY LEFT BLANK

LIST OF ACRONYMS AND ABBREVIATIONS

AI	artificial intelligence
AO	adaptive optics
CNN	convolutional neural network
DL	deep learning
GAN	generative adversarial network
HEL	high energy laser
ML	machine learning
PSF	point spread function
PSNR	peak signal-to-noise ratio
SSIM	structural similarity index measure
UAV	unmanned aerial vehicle

THIS PAGE INTENTIONALLY LEFT BLANK

ACKNOWLEDGMENTS

I would like to thank my advisors, Dr. Jae Jun Kim and Dr. Brij Agrawal, for guiding my research and their instruction in the topics of deep learning and adaptive optics. Their knowledge and experience were essential, and I would not have completed this research without their assistance. I would also like to thank Dr. Leonardo Herrera for lending his time and skills to help with code implementation.

Finally, thank you to my family and friends for their love and support. You have helped to shape the trajectory of my life that led me to this point.

THIS PAGE INTENTIONALLY LEFT BLANK

I. INTRODUCTION

High energy laser (HEL) platforms could prove to be a vital system for shipborne defense against unmanned aerial vehicles (UAVs) due to the HEL's high depth of magazine and low cost exchange ratio [1]. However, HEL systems must target specific locations on UAVs for optimal damage. This requirement results in the need for precise imaging of the target to determine optimal aimpoints. Image clarity is degraded by atmospheric turbulence between the HEL system and the target. To compensate for these atmospheric aberrations, current HEL systems use wavefront sensors and adaptive optics (AO) to measure the atmospheric aberration and alter the how the laser is focused. These systems are expensive to manufacture and add complexity to the HEL system. Advances in artificial neural networks provide the potential for compensating atmospheric aberrations without using complex wavefront sensors.

The purpose of this thesis is to investigate the use of deep learning models to compensate for atmospheric aberrations in UAV images. First, a performance baseline will be set by a classical deblurring technique called blind deconvolution. Then, the baseline performance will be compared to the performance of two state-of-the-art deep learning models called U-Net and DeblurGAN.

This thesis will begin with an overview of HEL systems, AO, and artificial intelligence (AI) and deep learning (DL) in Chapter II. Chapter III provides further context for how DL models can be applied for aberration compensation in HEL systems. The process of training and implementing the models will be covered in Chapter IV, and the results of the models' performance will be discussed in Chapter V. Finally, Chapter VI will summarize the completed research and provide direction for future work.

THIS PAGE INTENTIONALLY LEFT BLANK

II. BACKGROUND

A. HEL SYSTEM OVERVIEW

High energy lasers (HELs) are generally classified as lasers with power exceeding 1 kW. However, most tactical HELs in development operate on the magnitude of 10 kW to 100 kW while strategic-class HELs can exceed 1 MW in power output [2]. HEL systems could provide key advantages in shipboard defense in cost per shot and magazine depth. The cost of firing an HEL is the price of fuel needed to generate the required electricity, estimated at less than a dollar per shot. Conversely, conventional short-range air-defense missiles can cost hundreds of thousands of dollars each [3]. Similarly, surface ships can only carry a finite number of missiles and ammunition. Surface ships equipped with HEL systems would have a virtually unlimited magazine, constrained only by the ship's ability to generate sufficient electricity [3].

B. LIMITATIONS OF HEL SYSTEMS

While HEL systems provide advantages over conventional shipboard defense, they also have potential limitations. Lasers are sensitive to the atmosphere. Particles in the atmosphere such as water vapor, dust, and smoke scatter and absorb the laser light as it travels to its target. This atmospheric turbulence causes laser light to defocus, degrading the laser's effect on target [3]. Additionally, the HEL imaging system used for targeting is degraded by these atmospheric effects.

Thermal blooming is another limitation of HEL systems. When a laser fires continuously in one direction for an extended period, it heats up the air it passes through. The heated air defocuses the laser beam. This effect, known as thermal blooming, degrades the laser's ability to disable its intended target [4]. This study will focus on methods to compensate for aberrations caused by atmospheric turbulence.

C. ADAPTIVE OPTICS

A further explanation of optics and adaptive optics is needed for this study, beginning with how light propagates through a medium. A point source of light emits a

light wave in a spherical wavefront. According to the Huygen's Principle, "…all points of a wave front of sound in a transmitting medium or of light in a vacuum or transparent medium may be regarded as new sources of wavelets that expand in every direction at a rate depending on their velocities" [5]. This principle is illustrated in Figure 1. Each point on the wavefront acts as a secondary point source.

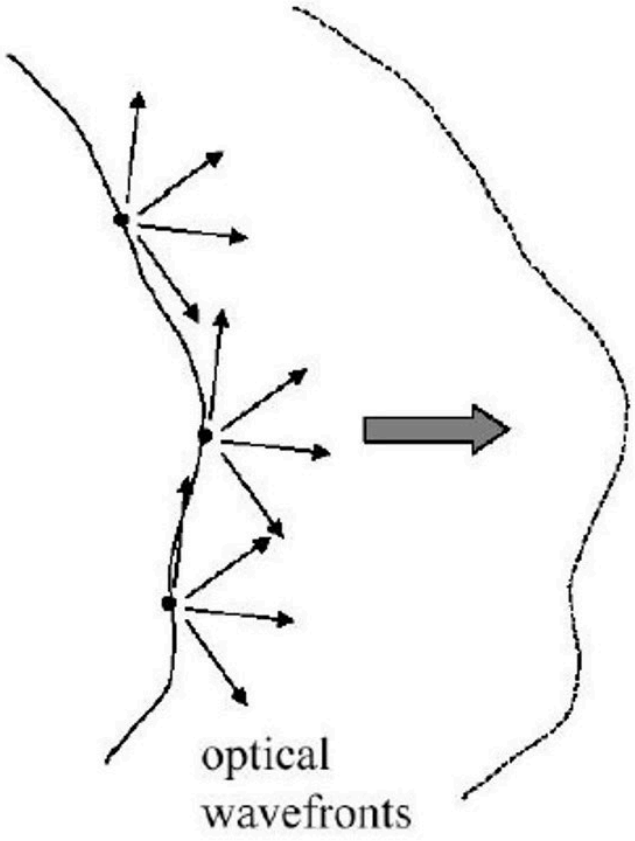

Figure 1. Wavefront Propagation. Source: [6].

In an ideal case, with no atmospheric disturbance, a wavefront from a point source propagates outward as a perfect sphere. As shown in Figure 2, when imaging light from a point source very far away, the wavefront will be a plane.

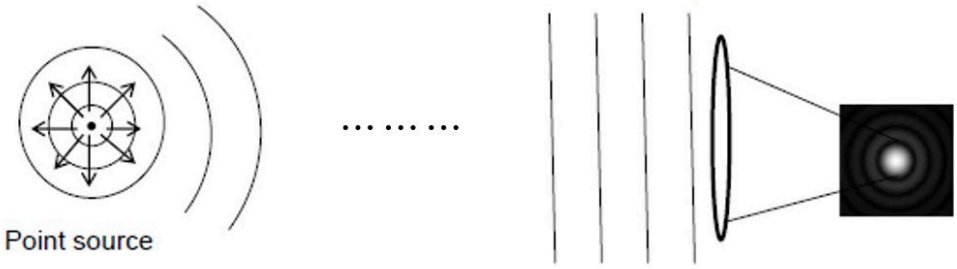

Figure 2. Point Source Image without Atmospheric Turbulence. Source: [6].

With a perfect lens, the light can be focused into an image of the original point source. However, because the light is diffracted by the lens, the image will take the form of an "airy disk" instead of a single point. The diffraction limit, defined in Equation (1.1), represents the spot size of the "airy disk" where D is the diameter of the lens and λ is the wavelength of the light [6].

$$\boldsymbol{\theta = 1.22\frac{\lambda}{D}} \tag{1.1}$$

When a wavefront propagates through the atmosphere, it is affected by turbulence. The aberrated wavefront is no longer a plane when it reaches the lens. As displayed in Figure 3, the resulting airy disk is distorted.

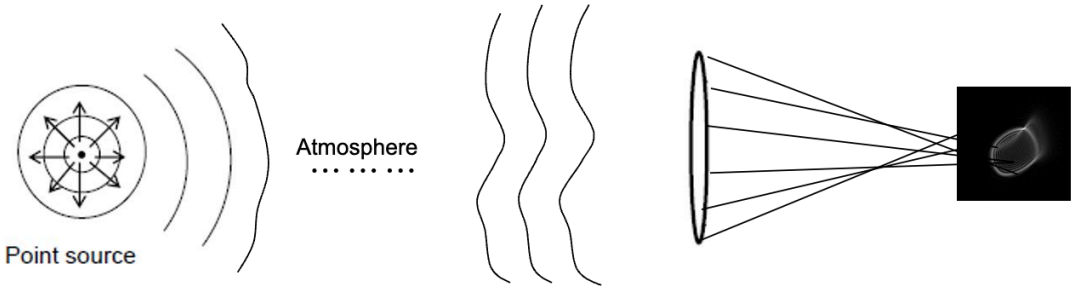

Figure 3. Point Source Image with Atmospheric Turbulence. Source: [6].

Adaptive optics (AO) improve the capability of optical systems by actively compensating for aberrations in real-time. Figure 4 shows how AO improves the performance of an optics system.

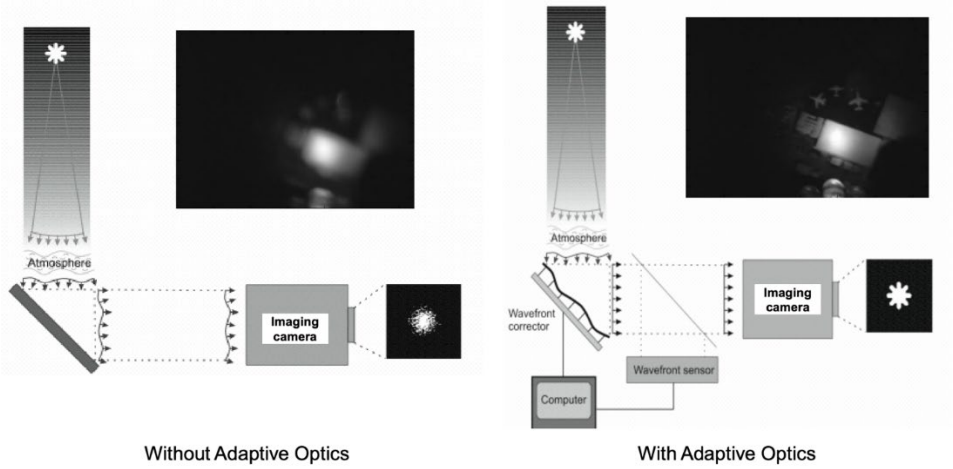

Figure 4. Example of Turbulence Effects on Telescope Images without (left) and with AO (right). Source: [7].

The wavefront sensor measures the shape of the wavefront and sends the information to the wavefront corrector, which is a deformable mirror. The mirror adapts its shape to correct the aberrations and create a new flat wavefront [7], [8].

While effective at compensating for atmospheric aberrations, AO systems add complex hardware requirements to HELs. Wavefront sensors are also limited in resolution and dynamic range and often requires a reference beacon. Artificial neural networks could be uniquely suited to overcome these limitations by compensating for aberrations without the need for additional hardware. Specifically, AI networks could estimate the incoming wavefront directly from the target image and use that information to correct target image and the laser beam.

D. ARTIFICIAL INTELLIGENCE AND DEEP LEARNING

Image correction algorithms exist that can apply aberration compensation directly to target images without having to measure the wavefront explicitly. Classically, blind deconvolution algorithms were used for post-processing of target images. However, the advent of deep learning algorithms such as convolutional neural networks (CNNs) and generative adversarial networks (GANs) have opened the possibility to create more

generalized image-correction models that can operate in near real-time. Chapter III will describe in greater detail the use of AI and deep learning for HEL systems applications.

E. RESEARCH OBJECTIVES

The objective of this research is to investigate two different deep learning approaches for correction of aberrated target images due to atmospheric turbulence. Image correction models based on U-Net and DeblurGAN architectures are developed using the simulated UAV target images under varying turbulence conditions. Performance of the resulting deep learning models are compared with the conventional image processing approach based on the blind deconvolution method. Based on this comparison study, the performance and further improvement areas are identified for deep learning methods applied to the atmospheric turbulence compensation problem.

THIS PAGE INTENTIONALLY LEFT BLANK

III. APPLICATIONS OF AI IN HEL SYSTEMS

This chapter will describe in detail how artificial intelligence (AI) can be applied to HEL systems to compensate for atmospheric aberrations. By performing aberration compensation directly on the target image, AI deblurring algorithms eliminate the need for a wavefront sensor. Additionally, the deblurred image will improve target tracking and aimpoint selection by providing a clearer view of the target.

A. REVIEW OF AI AND DEEP LEARNING

This section is an overview of the AI and deep learning topics relevant to this research. First the basics of AI and deep learning are discussed, followed by a more detailed explanation of neural networks and convolutional neural networks (CNNs).

1. AI, Machine Learning, Deep Learning

Artificial intelligence (AI) was defined in 1955 by Stanford Professor John McCarthy as, "the science and engineering of making intelligent machines" [9]. Since then, AI has developed broadly into numerous fields of science and engineering. Subsets of AI relevant to this research are machine learning (ML) and deep learning (DL). ML is a method used to model a system given some input data. ML is particularly useful when attempting to model complex systems that cannot easily be defined by equations and mathematical laws. Figure 5 outlines the general ML process. DL is subset of ML that employs a model known as a deep neural network.

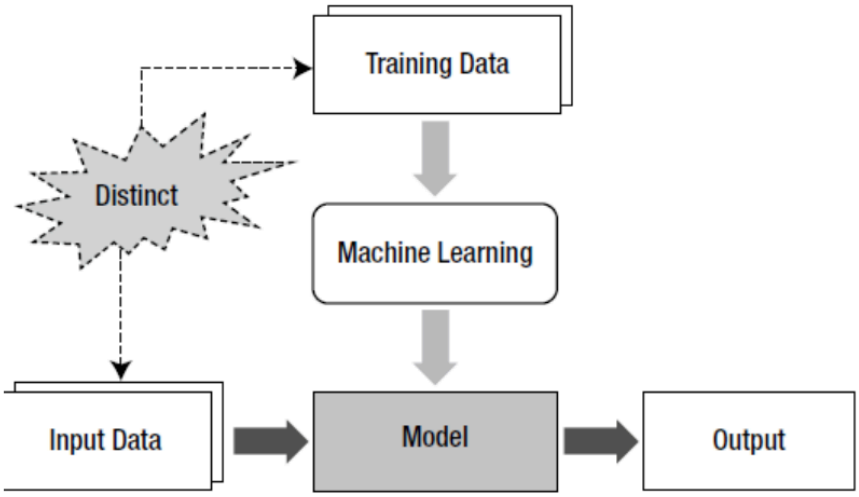

Figure 5. Machine Learning Process. Source: [10].

2. Neural Networks

The most widespread ML technique is the neural network. Based on the architecture of the human brain, neural networks are designed to allow computer programs to recognize patterns and improve themselves over time [11]. A neural network is a collection of node layers, with the outputs of one node layer becoming the inputs of the next node layer.

The neuron, or node, is the most basic building block of a neural network. Figure 6 illustrates the node's structure.

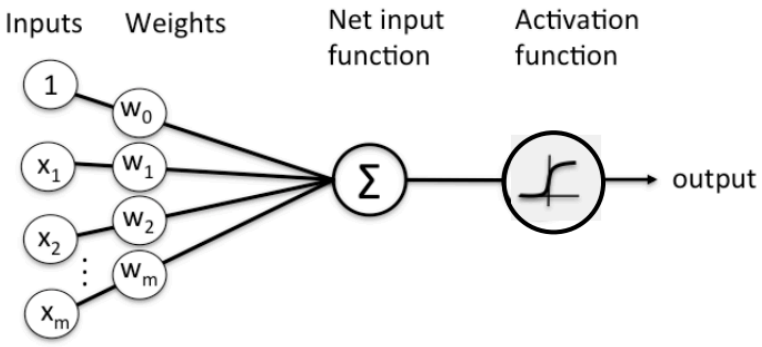

Figure 6. Node Design Structure. Source: [10].

The node's data inputs are multiplied by each individual weight and then summed together. A non-linear activation function is applied to the result. If the result's value is below the threshold set by the activation function, the node does not pass data to the next layer. If the value is above the threshold, the data will be transmitted to the next layer [10].

The operations performed by the node are described by the following equations summarized from [10]:

$$\boldsymbol{v = wx} \tag{1.2}$$

$$\boldsymbol{y = \varphi(v)'} \tag{1.3}$$

where v is the net input function before the activation function is applied, $\varphi(v)$ is the activation function, y is the node output, and $\boldsymbol{w}$ and $\boldsymbol{x}$ are vectors defined as followed.

$$\boldsymbol{w = [w_1\ w_2\ w_3\ \ldots\ w_n]} \tag{1.4}$$

$$\boldsymbol{x = \begin{bmatrix} x_1 \\ x_2 \\ x_3 \\ \vdots \\ x_n \end{bmatrix}} \tag{1.5}$$

While there are numerous types of activation functions, the rectified linear unit (ReLu) function is the most commonly used in deep neural networks due to its low computation cost and resilience against saturation [12]. The ReLu activation function is defined in Equation (1.6).

$$\boldsymbol{\varphi(v) = \begin{cases} 0, if\ v < 0 \\ v, if\ v \geq 0 \end{cases}} \tag{1.6}$$

Neural networks consist of tens to millions of nodes all interconnected from the input layer to the output layer. As shown in Figure 7, a deep neural network is simply a neural network with two or more hidden layers [10]. The neural networks relevant to this research are deep neural networks based on the convolutional neural network (CNN) architecture.

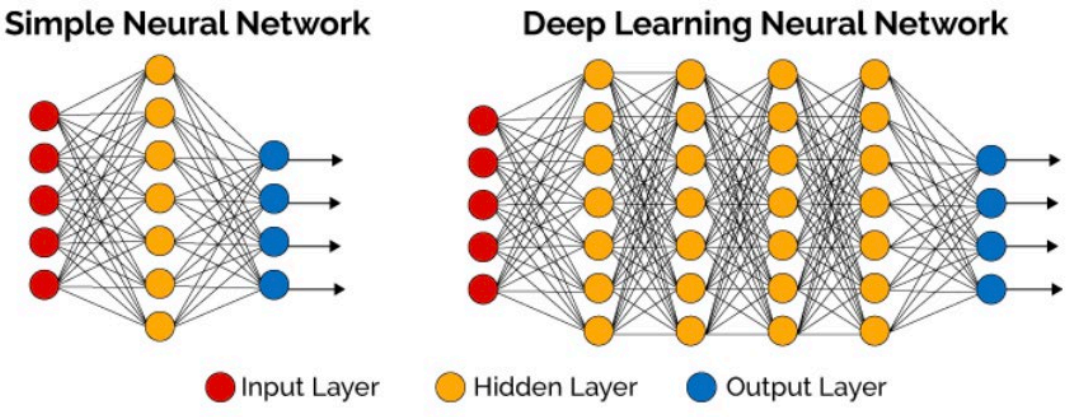

Figure 7. Simple Neural Network and Deep Neural Network. Source: [10].

3. Convolutional Neural Network

CNNs are a type of deep neural network designed to process data with a grid pattern to adaptively learn spatial hierarchies of features. This design enables CNNs to effectively process image data. CNNs consist of three layer-types: convolution, pooling, and fully connected layers [13]. The convolution layer performs feature extraction by constructing feature maps from an input image. Figure 8 displays a general convolution layer design.

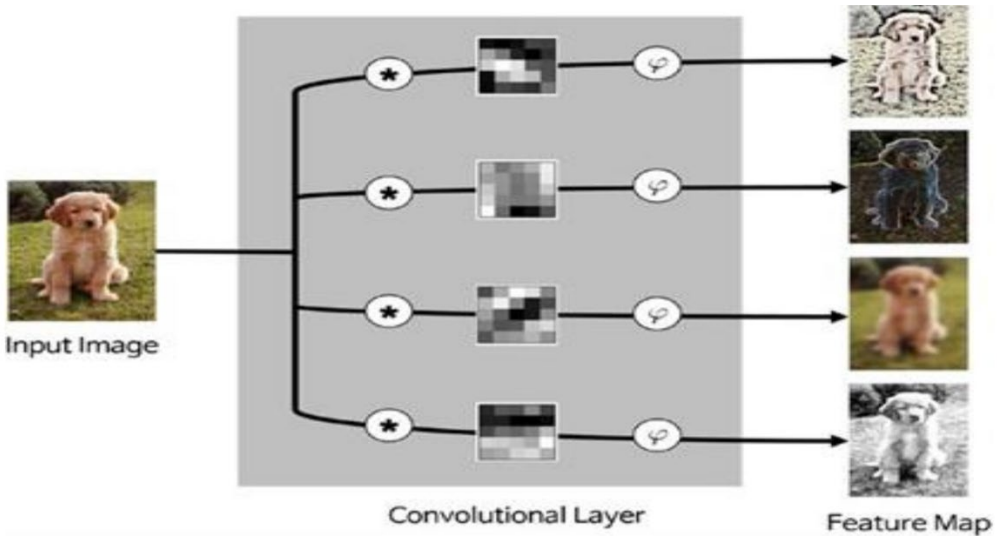

Figure 8. Convolution Layer Architecture. Source: [10].

The convolution layer contains convolution filters denoted by the square greyscale images in Figure 8. A convolution operation is performed on the input image and the convolution filters, and the results are sent through the activation function to create the feature maps. Pooling layers reduce the image size by combining adjacent pixels in a certain area into a single value. As a result, the pooling process decreases computational load and helps prevent overfitting. The final layer in a CNN is typically a fully connected layer, meaning every output from the previous layer is connected to every node of the final layer [13].

The two most common uses for CNNs are classification and regression. Classification networks are trained to determine which class the data belongs. A common classification example is a network that distinguishes between images of cats and dogs. The number of outputs of this network correlate to the number of classes being distinguished. Regression networks estimate a value based on the input data given. For example, given square footage and zip code of a building, a regression network could estimate the price of the building. More relevant to this research is image-to-image regression, in which the model attempts to augment a sample image to match a training image.

B. IMAGE ABERRATION COMPENSATION TECHNIQUES

This section provides a brief overview of the image aberration compensation methods used in this research: blind deconvolution, U-Net, and DeblurGAN.

1. Review of Blind Deconvolution

Blind deconvolution is a classical image restoration technique that does not use neural networks. Instead, blind deconvolution is an iterative process that attempts to find two unknown functions *h* and *g* knowing only their convolution *f*. The relationship between these functions is defined in Equation (1.7).

$$\boldsymbol{f(x,y) = h(x,y) * g(x,y) + b(x,y)} \tag{1.7}$$

where *f* is the blurred image, *h* is the unknown point spread function (PSF), *g* is the sharp latent image, and *b* is additive noise [14], [15].

A popular blind deconvolution algorithm for image reconstruction is the Richardson-Lucy algorithm developed by William Richardson and Leon Lucy in the 1970s [15]. The Richard-Lucy algorithm has been incorporated into a MATLAB function called deconvblind [16]. Deconvblind will be explored further in Chapter IV.

2. Review of U-Net

U-Net is a CNN originally designed to perform image segmentation on biomedical imagery. The network architecture of U-Net is essentially two CNNs, one that down-samples the input image and another that up-samples. As shown in Figure 9, the symmetrical architecture forms a u-shape [17].

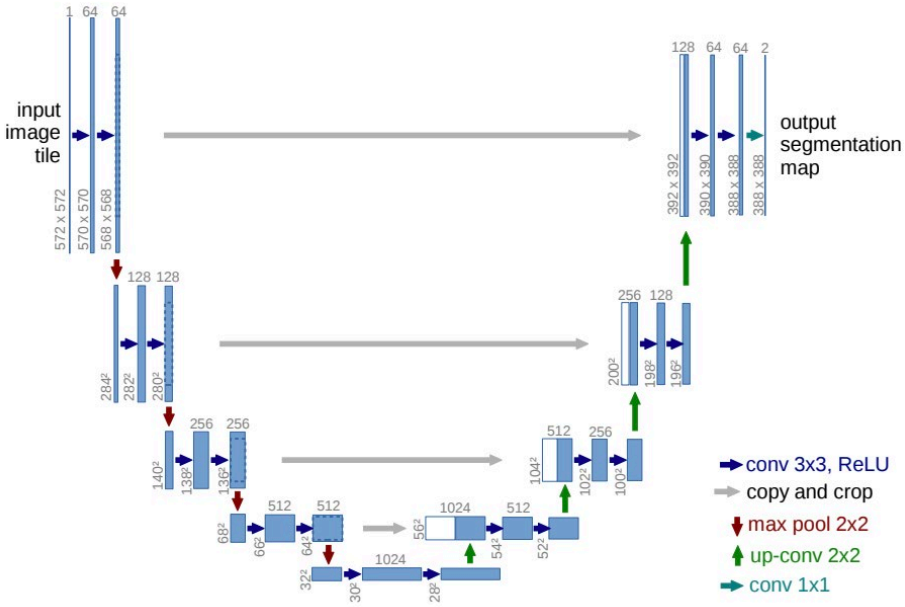

Figure 9. U-Net Architecture. Source: [17].

By connecting the corresponding levels of the down-sampler and up-sampler, U-Net benefits greatly from data augmentation, can train quickly, and requires a relatively

small dataset. This research modifies the original U-Net architecture to perform image-to-image regression.

3. Review of DeblurGAN

DeblurGAN is a type of generative adversarial network (GAN), a deep neural network designed to generate synthetic images similar to its training data. The original GAN architecture consists of two networks: the generator and the discriminator. The generator is trained to create images with high probabilities of being labelled as real images by the discriminator. The discriminator is trained to maximize the probability of correctly labelling real images and generated images [18]. The generator and discriminator train against each other until the discriminator is unable to distinguish between real and generated data.

In the original GAN architecture, the discriminator assigns a probability that a given image is real or fake with a value between zero and one. DeblurGAN replaces the discriminator with a critic model. The critic assigns a realness or fakeness score to the images, and trains to maximize the difference between the two score distributions. The difference between scores is known as the Wasserstein distance [14]. A basic DeblurGAN architecture for image deblurring is shown in Figure 10. The generator takes blurred images as inputs and outputs estimates of the sharp images. The critic compares the estimated restored images to the sharp images and computes the Wasserstein distance between them.

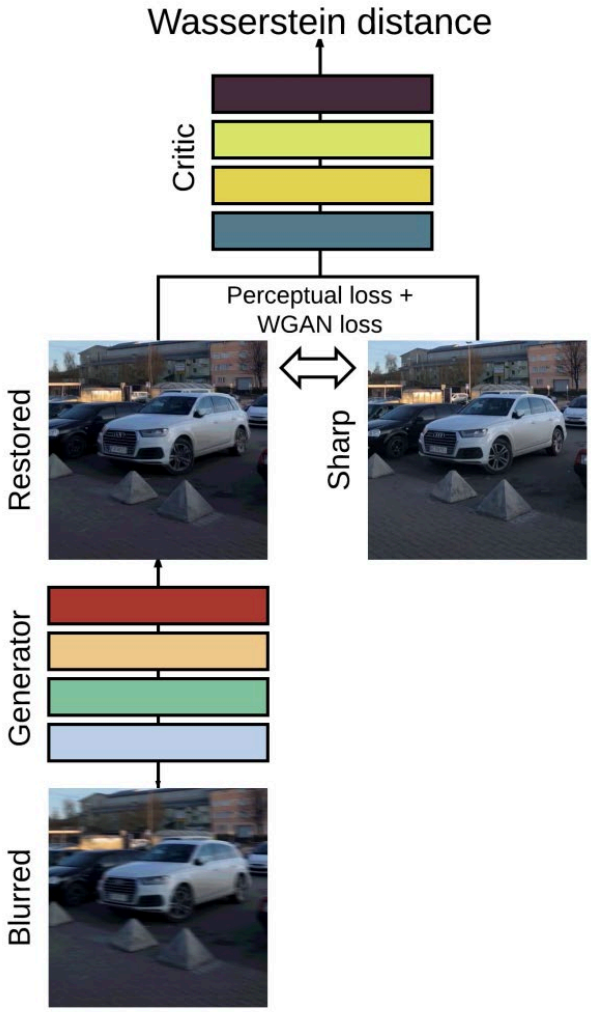

Figure 10. DeblurGAN Architecture. Source: [14].

IV. APPROACH OF STUDY

This chapter describes the methodologies used theories used to generate training data, train deep learning models, and quantify model performance. The chapter begins by working through how the image dataset was developed.

A. DATA GENERATION

To create a dataset consisting of pairs of images with and without atmospheric turbulence, the atmospheric turbulence needed to be simulated and applied to the pristine images. Zernike polynomials, polynomials defined on a unit circle, are commonly used to represent turbulent effects in the atmosphere. By randomizing the coefficients of the Zernike polynomials over a normal distribution, a polynomial representation of a wavefront can be generated [19]. Equation (1.8) defines the process of developing a wavefront, w, from Zernike polynomials, z_i, mathematically

$$\boldsymbol{w(r,\theta) = \sum_{i=1}^{\infty} a_i z_i(r,\theta)} \tag{1.8}$$

where a_i is the normally distributed coefficient, r is radial distance, and θ is azimuthal angle [19]. By transforming the wavefront in Equation (1.9) using a Fourier transform, F, the wavefront is converted into PSF

$$\boldsymbol{h = |F[w]|^2} \tag{1.9}$$

where h is the PSF. By convolving h with the pristine image, f, the blurred image is created. Equation (1.10) represents this process mathematically

$$\boldsymbol{g = h * f} \tag{1.10}$$

where g is the blurred image.

Another value used to control the level of turbulence applied to the pristine images is the Fried parameter. The Fried parameter, R_0, "indicates the length over which the wavefront can be considered planar" [20]. Furthermore, atmospheric turbulence decreases

as the Fried parameter increases. By incorporating the Fried parameter into the dataset generation process, the intensity of atmospheric aberrations can be controlled [19].

The training dataset for this research was generated from a set of 10,000 images of a Mongoose UAV model with computer simulated backgrounds. These pristine images were treated as the ground truth when determining model performance. By using the process described above, originally developed by Jun Zhang in a related thesis [21], blurred versions of the original pristine images were created. The turbulence characteristics were determined by parameters in Table 1.

Table 1. Dataset Generation Parameters

Parameter	Value
Aperture Diameter (m)	0.3
Target Distance (m)	4,000
Fried Parameter (m)	0.05, 0.10
Wavelength (m)	1E-6
Zernike Polynomials	18
Grid Size	512x512

This process increased the dataset size to 20,000 images consisting of 10,000 blurred/pristine pairs. Overall, two datasets were produced: one set of images with a Fried parameter equal to 5 cm and another with a Fried parameter of 10 cm. Samples of the training datasets are shown in Figure 11.

Figure 11. Example of UAV Training Dataset

B. MODEL TUNING

This section details how the image aberration compensation models were controlled to improve their performance on the training dataset.

1. Deconvblind

Deconvblind is a MATLAB function designed to deblur images using blind deconvolution, and is defined in Equation (1.11),

$$[\boldsymbol{J}, \boldsymbol{psfr}] = \boldsymbol{deconvblind}(\boldsymbol{I}, \boldsymbol{psfi}, \boldsymbol{iter}, \boldsymbol{weight}) \tag{1.11}$$

where the inputs are *I* (the initial image), *psfi* (the initial estimate of the PSF), *iter* (the number of iterations), and *weight* (determines how heavily each pixel is considered). The outputs are *J* (the deblurred image) and *psfr* (the PSF of the deblurred image) [22].

The initial images fed into the deconvblind function were the blurred images from the training dataset. The initial estimate of the PSF was a gaussian filter with the same size as the input image. 35 iterations were determined to provide the best overall performance. To compensate for any "ringing" in the restored image, the weight was set to assign the pixels around areas of high contrast to zero.

2. U-Net

The U-Net model used in this research was a modified version of the MATLAB U-Net implementation. Originally designed for image segmentation, this U-Net model had 58 layers [23]. To modify the model for image-to-image regression, the final two layers (a softmax activation layer and a segmentation layer) were replaced by a regression layer. In addition to modifying the model's layers, data augmentation was also performed on the image dataset to further improve the performance of the model. The dataset images were randomly rotated and reflected to increase the image variation. Table 2 displays the hyperparameters used for training the model.

Table 2. U-Net Hyperparameters

Hyperparameter	Value
Learning Rate	1E-5
Epochs	10
Mini-Batch Size	64
Encoder Depth	4

3. DeblurGAN

The DeblurGAN model used in this research was initially developed by Orest Kupyn et al. for image motion deblurring [14]. DeblurGAN consists of two models, the generator and the critic. The generator takes the blurred images from the training dataset as its inputs and outputs estimated restored images. The critic takes the estimated restored image and the pristine sharp image as inputs and outputs the difference between them. Table 3 shows the hyperparameters used during training.

Table 3. DeblurGAN Hyperparameters

Hyperparameter	Value	Notes (if any)
Learning Rate	1E-4	
Epochs	50	
Batch Size	16	
Critic Updates	5	Number of times the Critic is trained per epoch

C. PERFORMANCE METRICS

The images created by the three methods: blind deconvolution, U-Net, and DeblurGAN will be measured quantitatively by two metrics: peak signal-to-noise ratio (PSNR) and structural similarity index measure (SSIM). PSNR is one of the most widely used metrics to assess image quality, but it does not correlate well to the qualitative appearance of an image based on visual inspection. Conversely, SSIM is designed to correlate to the perceptual quality of an image [24].

1. Peak Signal-to-noise Ratio

The PSNR is, "an expression for the ratio between the maximum possible value (power) of a signal and the power of distorting noise that affects the quality of its representation" [25]. Specifically applied to images, PSNR can be defined by Equation (1.12)

$$\boldsymbol{PSNR = 10log_{10}\left(\frac{peakval^2}{MSE}\right)} \tag{1.12}$$

where *peakval* is the maximum pixel value of the reference image and *MSE* is the mean squared error between the reference image and the restored image [26]. *MSE* is defined by Equation (1.13)

$$\boldsymbol{MSE = \frac{1}{mn}\sum_0^{m-1}\sum_0^{n-1}\|f(i,j) - g(i,j)\|^2} \tag{1.13}$$

where *f* is the reference image, *g* is the restored image, *m* represents the number of rows of the images, *n* represents the number of columns of the images, *i* represents the row index,

and *j* represents the column index [25]. The larger the value of PSNR, the better the image quality.

2. Structural Similarity Index Measure

SSIM is an image quality metric that compares the luminance, contrast, and structure of two images. SSIM is defined mathematically by Equation (1.14)

$$\boldsymbol{SSIM}(\boldsymbol{x},\boldsymbol{y}) = [\boldsymbol{l}(\boldsymbol{x},\boldsymbol{y})]^{\boldsymbol{\alpha}} * [\boldsymbol{c}(\boldsymbol{x},\boldsymbol{y})]^{\boldsymbol{\beta}} * [\boldsymbol{s}(\boldsymbol{x},\boldsymbol{y})]^{\boldsymbol{\gamma}}$$

$$\boldsymbol{l}(\boldsymbol{x},\boldsymbol{y}) = \frac{\boldsymbol{2\mu_x\mu_y + C_1}}{\boldsymbol{\mu_x^2 + \mu_y^2 + C_1}}$$

$$\boldsymbol{c}(\boldsymbol{x},\boldsymbol{y}) = \frac{\boldsymbol{2\sigma_x\sigma_y + C_2}}{\boldsymbol{\sigma_x^2 + \sigma_y^2 + C_2}}$$

$$\boldsymbol{s}(\boldsymbol{x},\boldsymbol{y}) = \frac{\boldsymbol{\sigma_{xy}+C_3}}{\boldsymbol{\sigma_x\sigma_y+C_3}} \qquad (1.14)$$

where "μ_x, μ_y, σ_x, σ_y, and σ_{xy} are the local means, standard deviations, and cross-covariance for images *x, y*" [27]. The resulting value ranges from zero (completely different luminance, contrast, and structure) to one (identical luminance, contrast, and structure).

This research utilizes a multi-scale SSIM developed by Wang, Simoncelli, and Bovik [24]. Multi-scale SSIM is a more flexible version of SSIM that performs better on image data with variations in viewing condition. This increase in performance is obtained by iteratively scaling the images and taking multiple measurements of the contrast and structure of the images. Then, the luminance of the images is calculated at the final iteration. The multi-scale SSIM is evaluated by combining all the different measurements as shown in Equation (1.15)

$$\boldsymbol{SSIM}(\boldsymbol{x},\boldsymbol{y}) = [\boldsymbol{l_M}(\boldsymbol{x},\boldsymbol{y})]^{\boldsymbol{\alpha_M}} \prod_{\boldsymbol{j=1}}^{\boldsymbol{M}} \left[\boldsymbol{c_j}(\boldsymbol{x},\boldsymbol{y})\right]^{\boldsymbol{\beta_j}} \left[\boldsymbol{s_j}(\boldsymbol{x},\boldsymbol{y})\right]^{\boldsymbol{\gamma_j}} \qquad (1.15)$$

where *M* is the final iteration and *j* is the iteration index [24].

V. RESULTS

In this chapter, the results of the image restoration methods are presented. First, each method is studied individually starting with blind deconvolution, then U-Net, ending with DeblurGAN. Then, the three methods are compared to each other to determine which image restoration method is superior in terms of PSNR and SSIM. Each method was scored on a R_0 = 10cm dataset and an R_0 = 5cm dataset. The average PSNR and SSIM of 100 images were calculated on both uncropped and cropped versions of each image. Examples of the images tested are displayed in Figure 12.

Figure 12. Sample of Uncropped and Cropped Images

The cropped images focused the images on the UAV target. By eliminating most of the background, the images' performance metrics will be weighted towards how well the restored image restores the UAV structure.

A. DECONVBLIND RESULTS

Blind deconvolution achieved modest results in compensating for atmospheric aberrations when R_0 = 10cm. A sample of the restored images compared to the pristine images and blurred images is displayed in Figure 13.

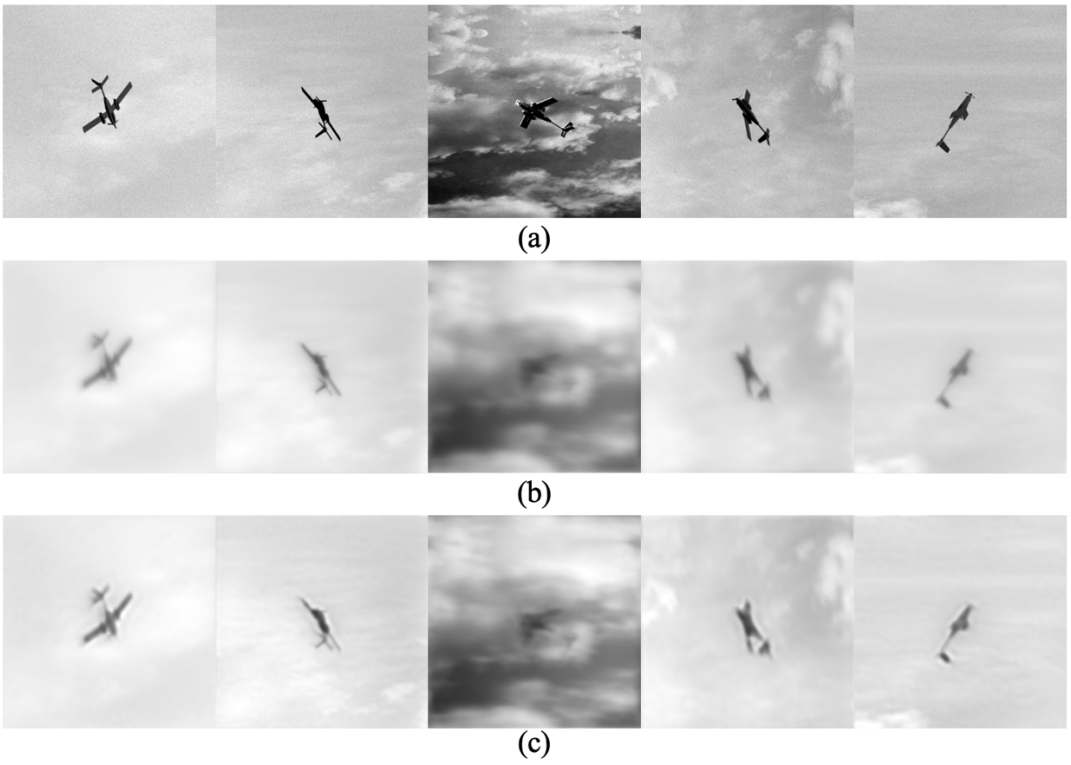

Figure 13. Sample of Pristine Images (a), Blurred Images with R_0 = 10cm (b), and Restored Images (c) Using Blind Deconvolution

The PSNR and SSIM between the pristine sharp image and the restored image were measured for 100 images, and an average PSNR and SSIM was calculated. The results were plotted for both uncropped and cropped images in Figure 14.

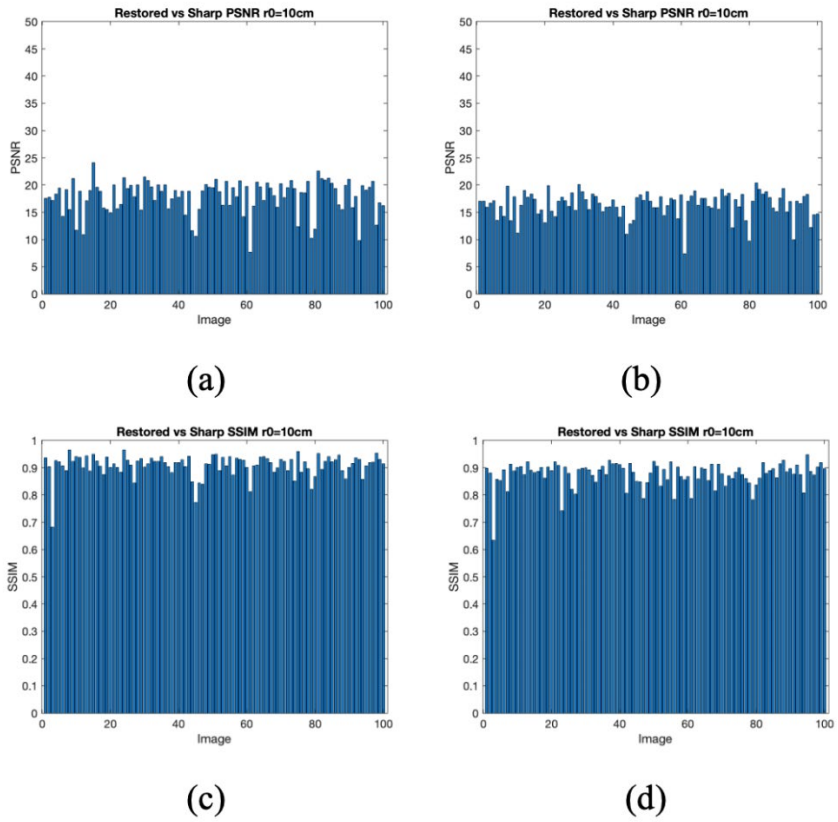

Figure 14. PSNR of Uncropped (a) and Cropped (b); SSIM of Uncropped (c) and Cropped (d) at R_0 = 10cm Using Blind Deconvolution

The average values of PSNR and SSIM are tabulated in Table 4.

Table 4. Average PSNR and SSIM when R_0 = 10cm Using Blind Deconvolution

	Average PSNR	**Average SSIM**
Uncropped	17.8727	0.9088
Cropped	16.3591	0.8752

The same process was repeated after changing the Fried Parameter to R_0 = 5cm. A sample of the resulting images is displayed in Figure 15.

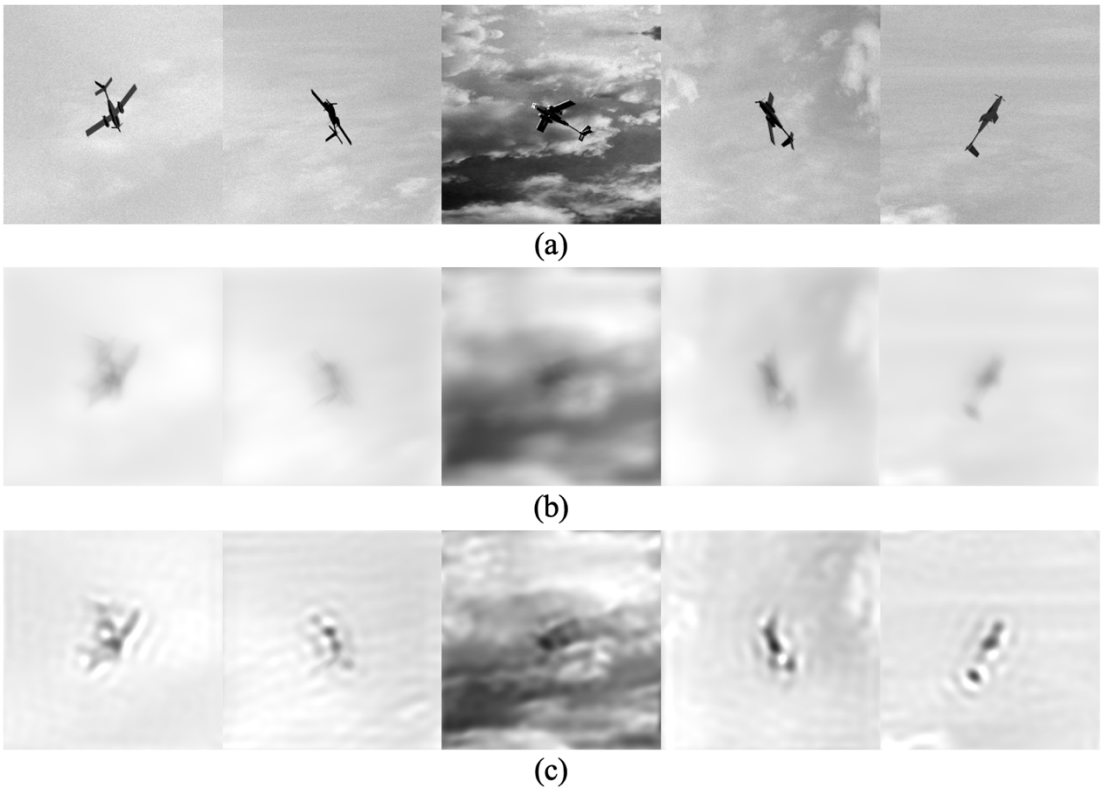

Figure 15. Sample of Pristine Images (a), Blurred Images with R_0 = 5cm (b), and Restored Images (c) Using Blind Deconvolution

Blind deconvolution's performance suffered when the atmospheric aberrations increased in intensity. The PSNR and SSIM values of the 100 images are illustrated by Figure 16.

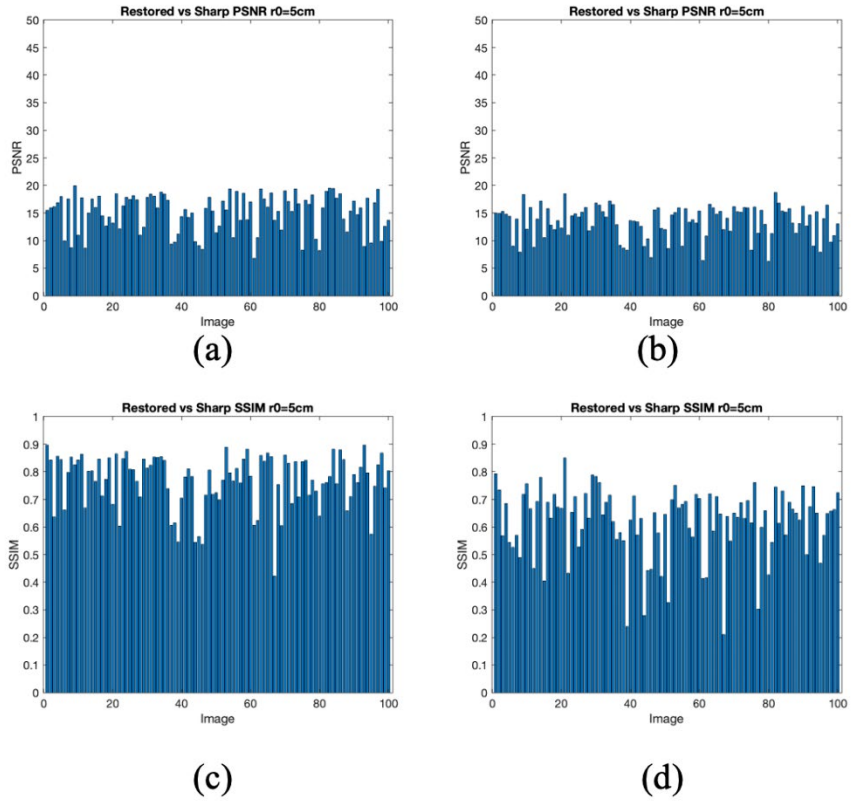

Figure 16. PSNR of Uncropped (a) and Cropped (b); SSIM of Uncropped (c) and Cropped (d) at R_0 = 5cm Using Blind Deconvolution

The average values of PSNR and SSIM are shown in Table 5.

Table 5. Average PSNR and SSIM when R_0 = 5cm Using Blind Deconvolution

	Average PSNR	**Average SSIM**
Uncropped	15.0199	0.7675
Cropped	13.4002	0.6169

B. U-NET RESULTS

After training the U-Net model, the model was validated on 100 images at both R_0 = 10cm and R_0 = 5cm. A sample of the restored images when R_0 = 10cm are displayed in Figure 17.

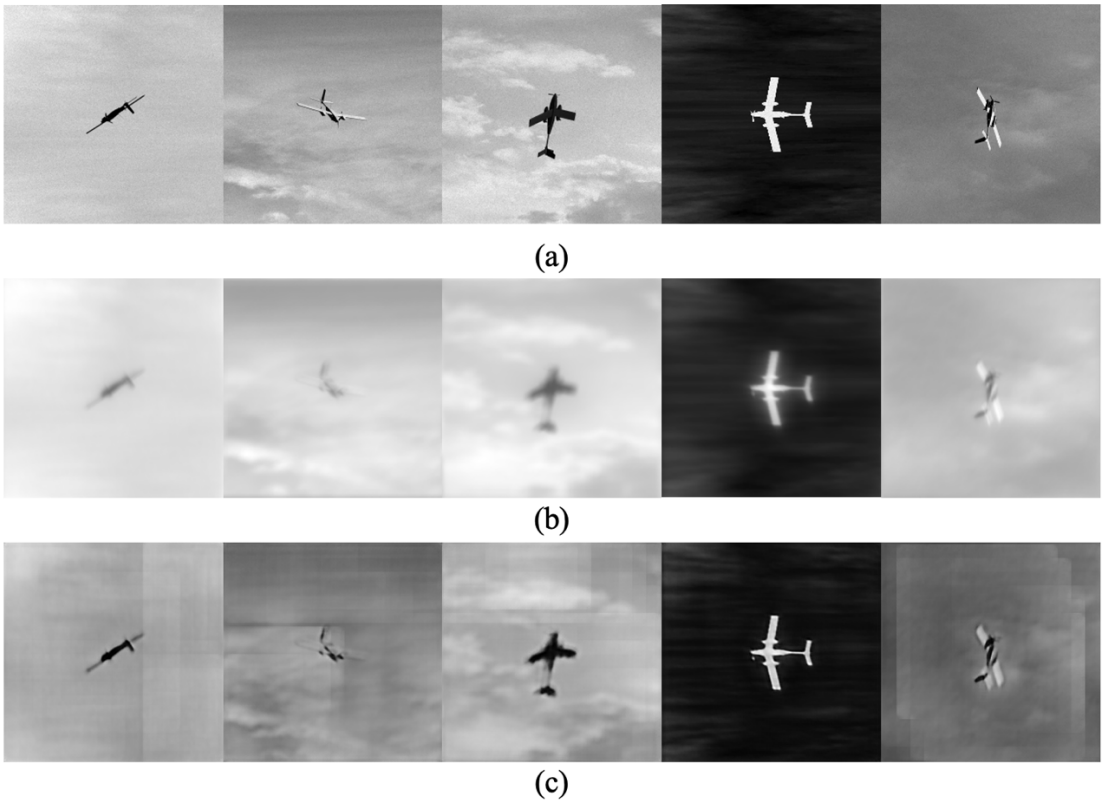

Figure 17. Sample of Pristine Images (a), Blurred Images with R_0 = 10cm (b), and Restored Images (c) Using U-Net

The PSNR and SSIM values of the 100 images are displayed in Figure 18.

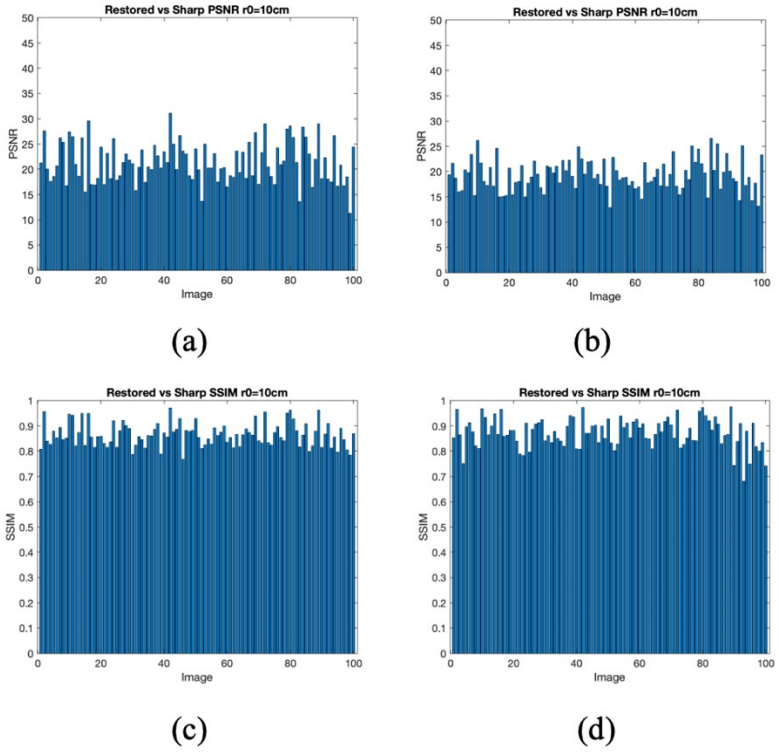

Figure 18. PSNR of Uncropped (a) and Cropped (b); SSIM of Uncropped (c) and Cropped (d) at R_0 = 10cm Using U-Net

The average PSNR and SSIM of the uncropped and cropped images are shown in Table 6.

Table 6. Average PSNR and SSIM when R_0 = 10cm Using U-Net

	Average PSNR	**Average SSIM**
Uncropped	21.4038	0.8654
Cropped	19.2831	0.8726

The Fried Parameter was changed to R_0 = 5cm and the process was repeated. A sample of the results is displayed in Figure 19.

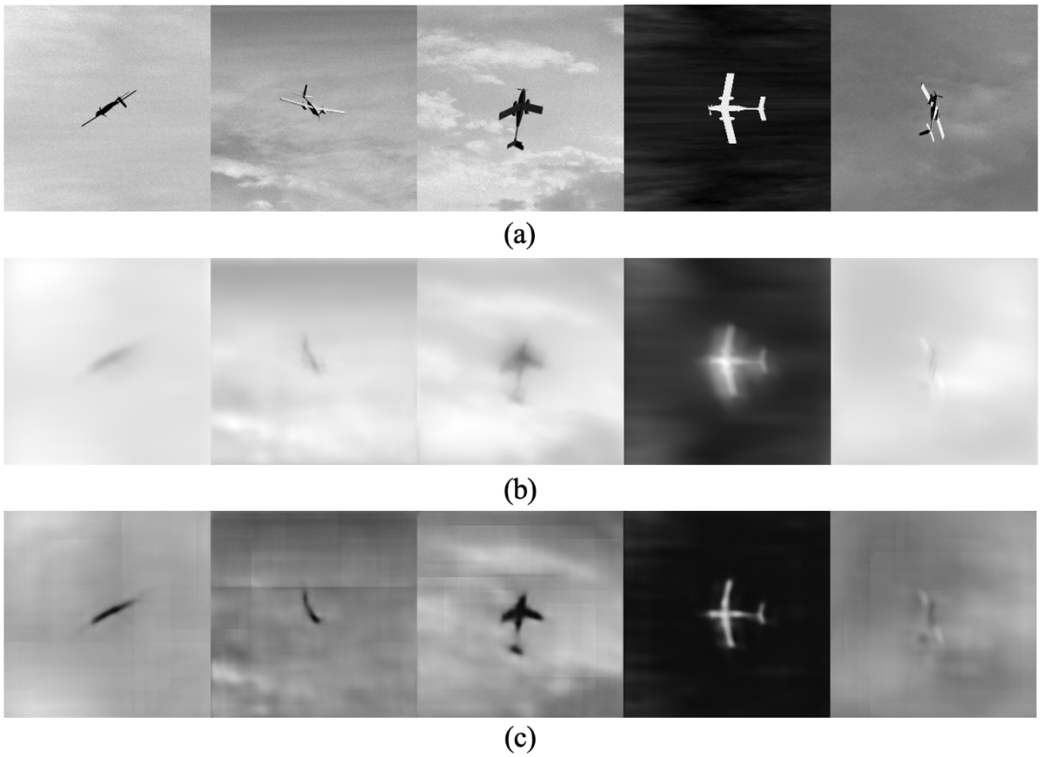

Figure 19. Sample of Pristine Images (a), Blurred Images with R_0 = 5cm (b), and Restored Images (c) Using U-Net

The PSNR and SSIM values of the 100 images are shown in Figure 20.

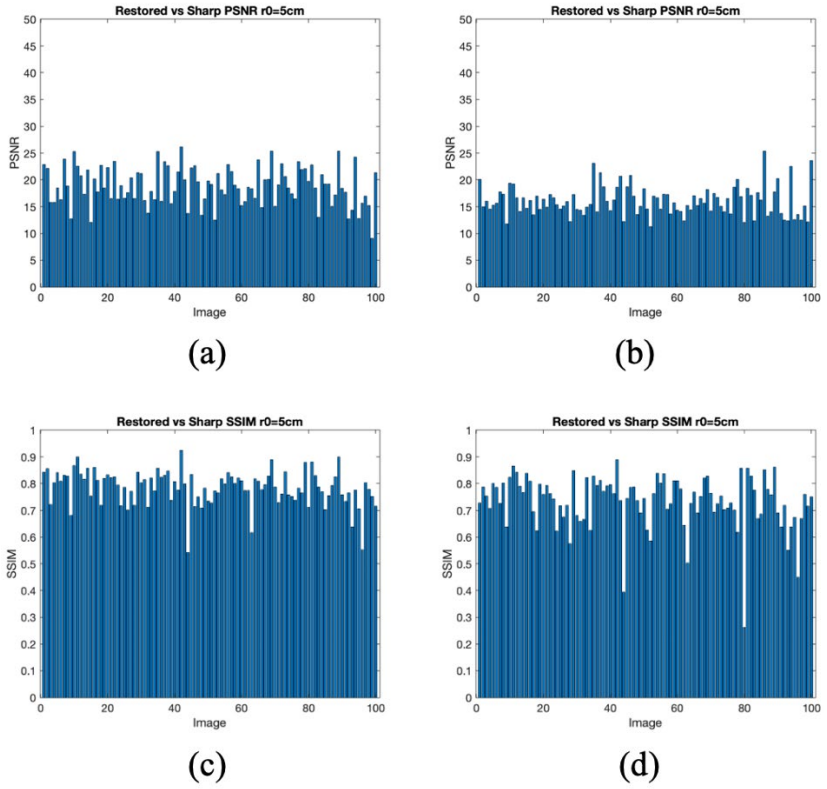

Figure 20. PSNR of Uncropped (a) and Cropped (b); SSIM of Uncropped (c) and Cropped (d) at R_0 = 5cm Using U-Net

The average PSNR and SSIM values are tabulated in Table 7.

Table 7. Average PSNR and SSIM when R_0 = 5cm Using U-Net

	Average PSNR	**Average SSIM**
Uncropped	18.8453	0.7848
Cropped	16.0244	0.7320

C. DEBLURGAN RESULTS

After training the DeblurGAN model, the model was validated on 100 images at both R_0 = 10cm and R_0 = 5cm. A sample of the restored images when R_0 = 10cm are displayed in Figure 21.

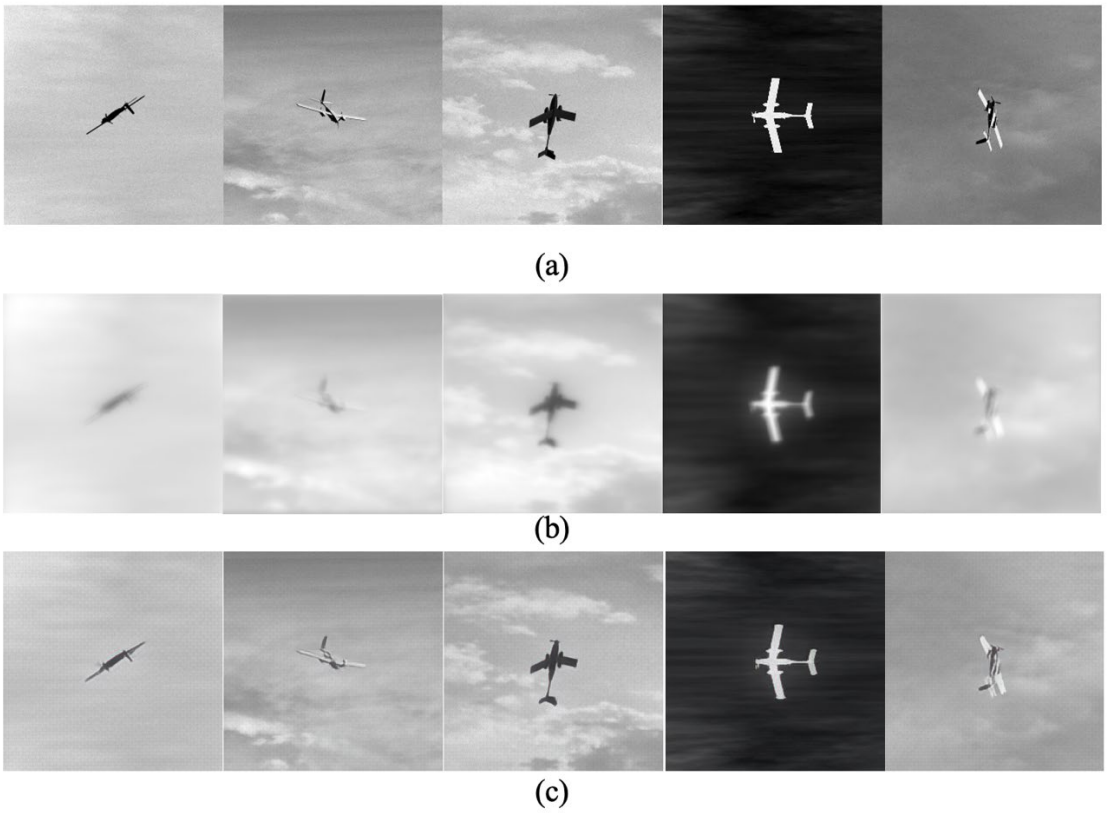

Figure 21. Sample of Pristine Images (a), Blurred Images with R_0 = 10cm (b), and Restored Images (c) Using DeblurGAN

The images restored by the DeblurGAN model qualitatively look very similar to the original pristine images. The PSNR and SSIM values for of the 100 images are displayed in Figure 22.

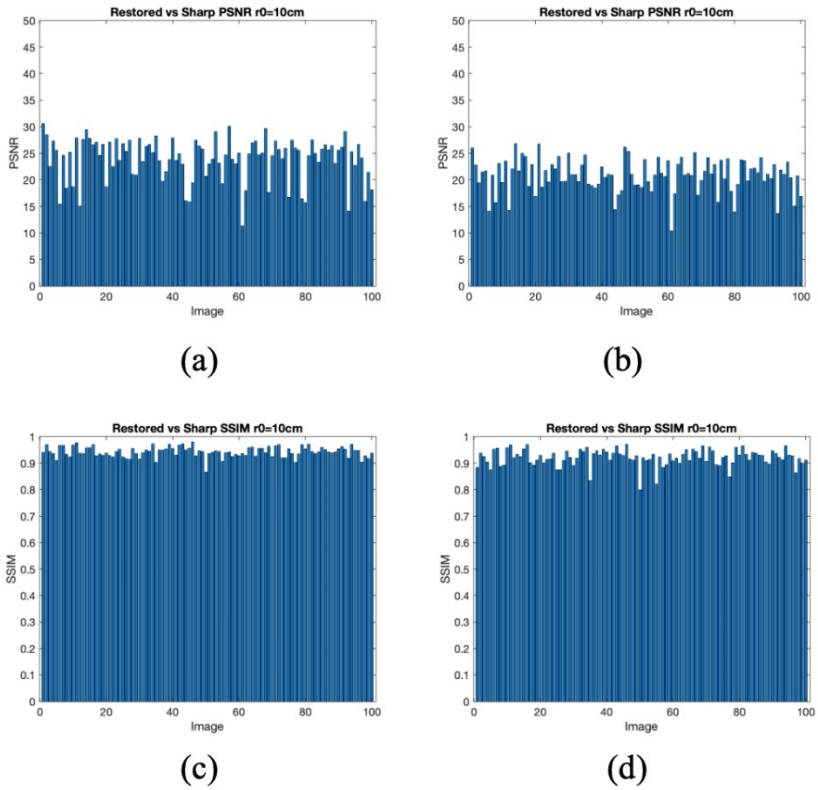

Figure 22. PSNR of Uncropped (a) and Cropped (b); SSIM of Uncropped (c) and Cropped (d) at R_0 = 10cm Using DeblurGAN

The average PSNR and SSIM are shown in Table 8.

Table 8. Average PSNR and SSIM when R_0 = 10cm Using DeblurGAN.

	Average PSNR	**Average SSIM**
Uncropped	22.7774	0.9427
Cropped	20.2256	0.9211

The process was repeated after changing the Fried Parameter to R_0 = 5cm. A sample of the resulting images are shown in Figure 23.

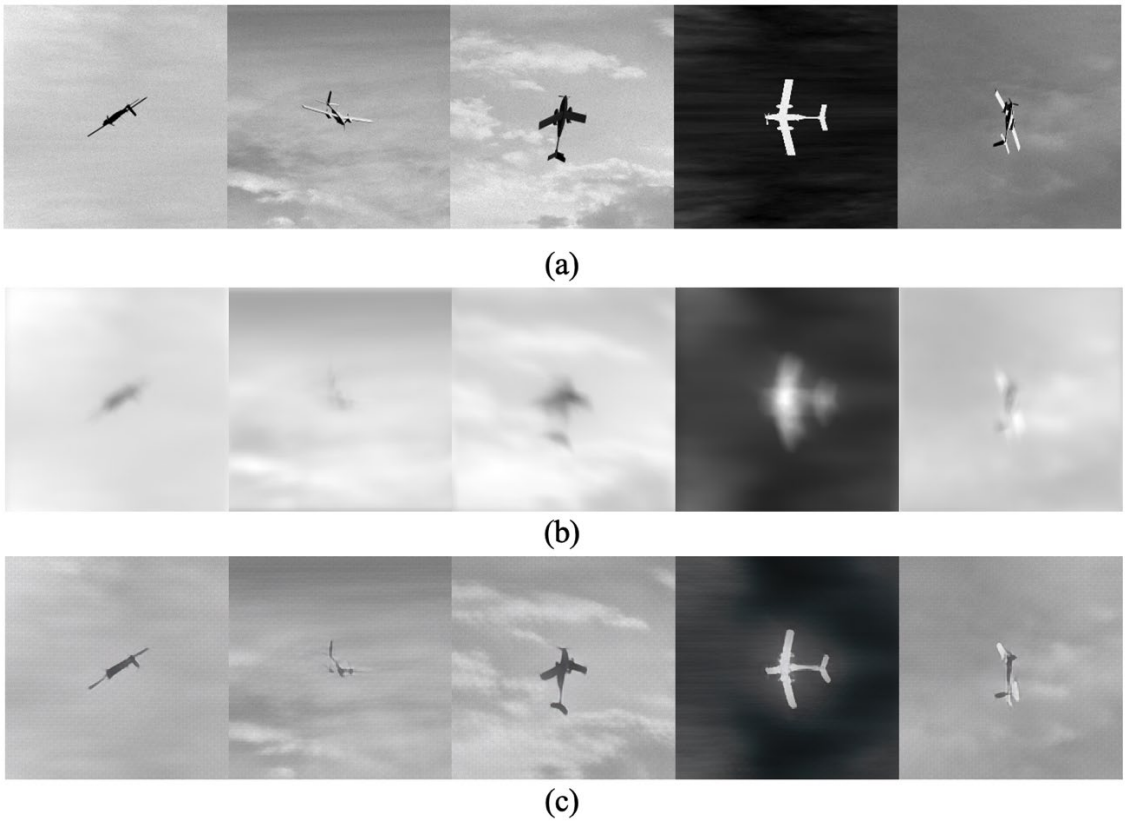

Figure 23. Sample of Pristine Images (a), Blurred Images with R_0 = 5cm (b), and Restored Images (c) Using DeblurGAN

The PSNR and SSIM values of the 100 images are shown in Figure 24.

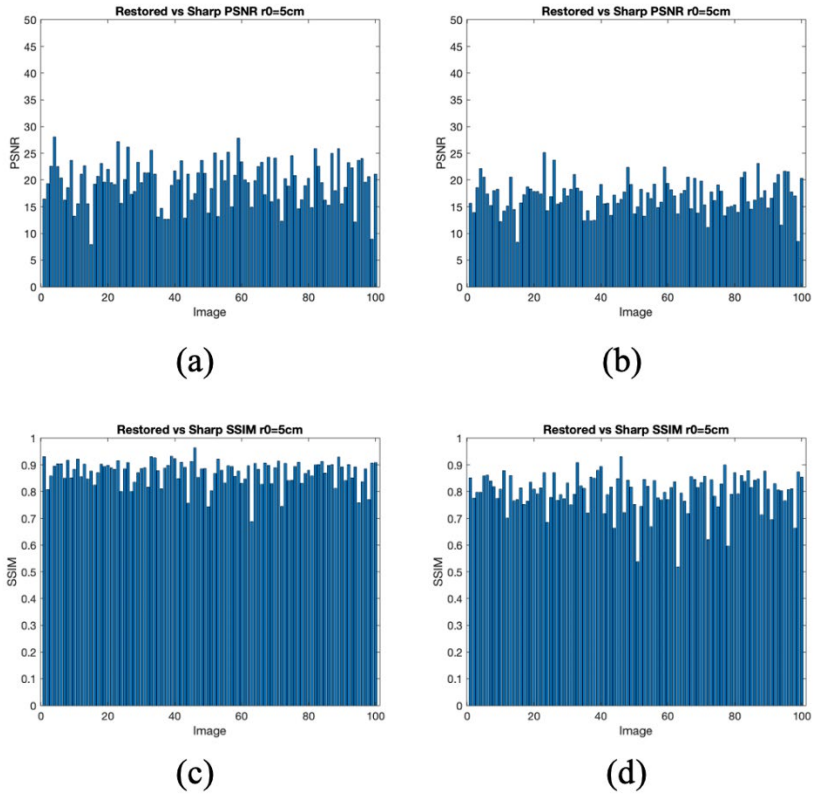

Figure 24. PSNR of Uncropped (a) and Cropped (b); SSIM of Uncropped (c) and Cropped (d) at R_0 = 5cm Using DeblurGAN

The average PSNR and SSIM values are displayed in Table 9.

Table 9. Average PSNR and SSIM when R_0 = 5cm Using DeblurGAN

	Average PSNR	**Average SSIM**
Uncropped	19.5652	0.8714
Cropped	17.0037	0.7969

D. MODEL COMPARISON

This section summarizes and compares the performance of the three image aberration compensation methods tested in this research. The two deep learning models (U-Net and DeblurGAN) dramatically outperformed blind deconvolution when comparing PSNR values. As illustrated in Table 10, DeblurGAN ranked first in all categories of images tested. U-Net scored closely behind DeblurGAN, while blind deconvolution fell far below the other two models.

Table 10. Average PSNR Value Summary

	R_0 = 5cm		R_0 = 10cm	
	Uncropped	**Cropped**	**Uncropped**	**Cropped**
Blind Deconvolution	15.0199	13.4002	17.8727	16.3591
U-Net	18.8453	16.0244	21.4038	19.2831
DeblurGAN	**19.5652**	**17.0073**	**22.7774**	**20.2256**

While the deep learning models clearly outperformed blind deconvolution in terms of PSNR. The results are more nuanced when comparing SSIM values. Table 11 shows DeblurGAN still dramatically outperformed the other two methods, but blind deconvolution scored higher than U-Net when the Fried parameter was R_0 =10cm.

Table 11. Average SSIM Value Summary

	R_0 = 5cm		R_0 = 10cm	
	Uncropped	**Cropped**	**Uncropped**	**Cropped**
Blind Deconvolution	0.7675	0.6169	0.9088	0.8752
U-Net	0.7848	0.7320	0.8654	0.8726
DeblurGAN	**0.8714**	**0.7969**	**0.9427**	**0.9211**

By studying the visual appearance of the restored images, the SSIM scores begin to make more since. As detailed in Chapter IV, SSIM uses the luminance, contrast, and structure of images to calculate how visually similar they appear. As shown in Figure 25,

the images restored by the DeblurGAN model are clearly the most similar visually to the pristine images. The most likely reason U-Net underperformed in SSIM is the slightly pixelated artifacts seen in the restored images.

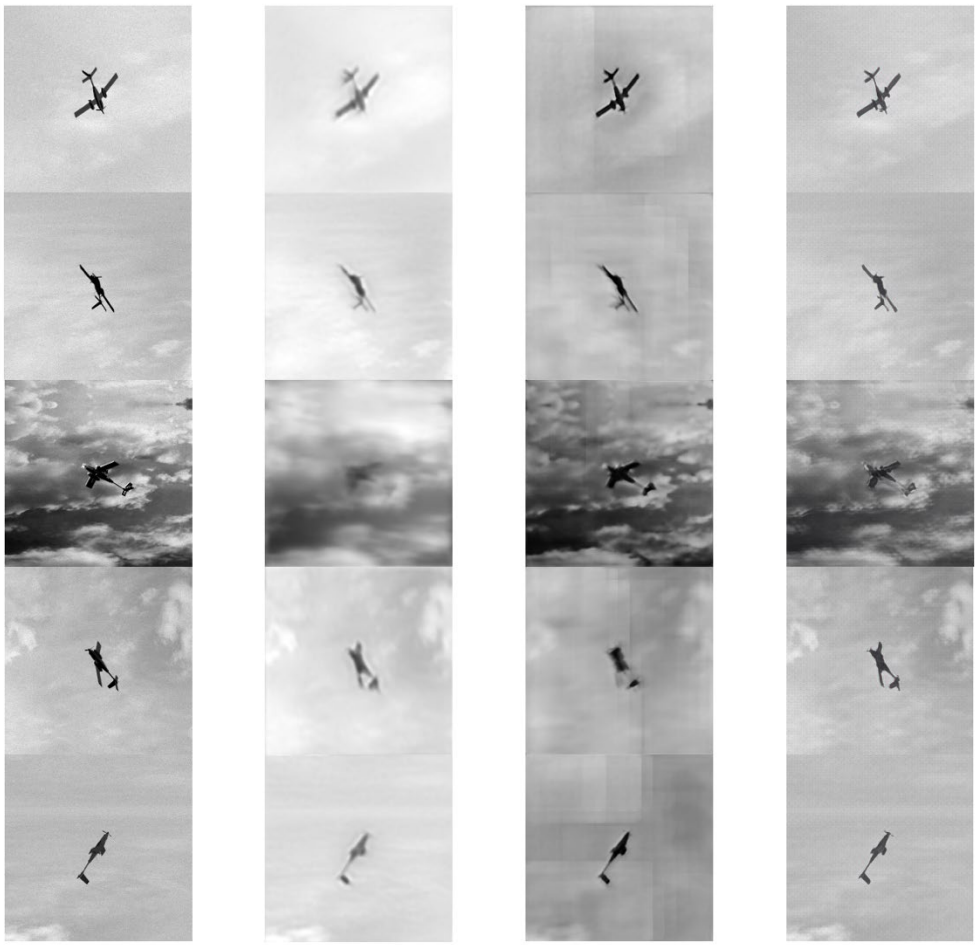

Figure 25. Visual Comparison of Image Correction Methods When R_0 =10cm. Pristine Image (a), Blind Deconvolution (b), U-Net (c), DeblurGAN (d)

THIS PAGE INTENTIONALLY LEFT BLANK

VI. CONCLUSION

The results of this study show that deep learning models are highly effective at compensating for atmospheric aberrations and outperformed conventional methods when tested on simulated UAV target image data. These image aberration compensation methods can improve the performance of HEL systems by estimating wavefronts directly from target images and using the data to correct the target image and the laser beam.

Blind deconvolution, U-Net, and DeblurGAN algorithms were tested on simulated UAV datasets with Fried parameter values of R_0 =5cm and R_0 =10cm. The resulting restored images were compared to the pristine dataset and scored on PSNR and SSIM. Overall DeblurGAN had the highest performance, achieving the highest PSNR and SSIM scores. The images generated by DeblurGAN were also the most similar to the pristine images qualitatively, based on visual inspection.

DeblurGAN should be studied further in future work to determine its effectiveness on real-world data. A larger and more diverse dataset could dramatically improve the model's performance in image aberration compensation tasks.

THIS PAGE INTENTIONALLY LEFT BLANK

LIST OF REFERENCES

[1] R. O'Rourke, "Navy Lasers, Railgun, and Gun-Launched Guided Projectile: Background and Issues for Congress," Washington, DC, USA, CRS Report No. R44175, 2022 [Online]. Available: https://sgp.fas.org/crs/weapons/R44175.pdf

[2] A. Angell, "The High-Energy Laser: Tomorrow's Weapon to Improve Force Protection," Defense Technical Information Center, Fort Belvoir, VA, 2012 [Online]. Available: https://apps.dtic.mil/sti/citations/ADA562311

[3] R. O'Rourke, "Navy Shipboard Lasers for Surface, Air, and Missile Defense: Background and Issues for Congress," Washington, DC, USA CRS Report No. R41526, 2015 [Online]. Available: http://public1.nhhcaws.local/research/library/online-reading-room/title-list-alphabetically/n/navy-shipboard-lasers.html

[4] D. C. Smith, "High-power laser propagation: Thermal blooming," Proceedings of the IEEE, vol. 65, no. 12, pp. 1679–1714, Dec. 1977, doi: 10.1109/PROC.1977.10809.

[5] Encyclopaedia Britannica, "Huygens' principle," [Online]. Available: https://www.britannica.com/science/Huygens-principle

[6] J. J. Kim, "Background Tutorial," class notes for Applications of Deep Learning for Military Systems, Dept. of Mech. and Aero. Eng., Naval Postgraduate School, Monterey, CA, USA, fall 2022.

[7] J. J. Kim, "AE4818 Set 5 Optical Beam Control," class notes for Acquistion, Tracking, and Pointing of Military Spacecraft, Dept. of Mech. and Aero. Eng., Naval Postgraduate School, Monterey, CA, USA, winter 2022.

[8] M. Aftab, H. Choi, R. Liang, and D. W. Kim, "Adaptive Shack-Hartmann wavefront sensor accommodating large wavefront variations," Opt. Express, OE, vol. 26, no. 26, pp. 34428–34441, Dec. 2018, doi: 10.1364/OE.26.034428.

[9] Stanford University Human-Centered Artificial Intelligence, *Artificial Intelligence Definitions*, 2020 [Online]. Available: https://hai.stanford.edu/sites/default/files/2020-09/AI-Definitions-HAI.pdf

[10] B. Agrawal, "AE 4824–22," class notes for Applications of Deep Learning for Military Systems, Dept. of Mech. and Aero. Eng., Naval Postgraduate School, Monterey, CA, USA, fall 2022.

[11] IBM, "What are Neural Networks?," August 17, 2020 [Online]. Available: https://www.ibm.com/cloud/learn/neural-networks

[12] DeepAI, “ReLu,” May 17, 2019 [Online]. Available: https://deepai.org/machine-learning-glossary-and-terms/relu

[13] R. Yamashita, M. Nishio, R. K. G. Do, and K. Togashi, “Convolutional neural networks: an overview and application in radiology,” Insights Imaging, vol. 9, no. 4, Art. no. 4, Aug. 2018, doi: 10.1007/s13244-018-0639-9.

[14] O. Kupyn, V. Budzan, M. Mykhailych, D. Mishkin, and J. Matas, “DeblurGAN: Blind Motion Deblurring Using Conditional Adversarial Networks,” arXiv:1711.07064 [cs], Apr. 2018 [Online]. Available: http://arxiv.org/abs/1711.07064

[15] H. Lanteri, C. Aime, H. Beaumont, and P. Gaucherel, “Blind deconvolution using the Richardson-Lucy algorithm,” in Optics in Atmospheric Propagation and Random Phenomena, Dec. 1994, vol. 2312, pp. 182–192. doi: 10.1117/12.197374.

[16] MATLAB, “Deblur image using blind deconvolution - MATLAB deconvblind.” [Online]. Available: https://www.mathworks.com/help/images/ref/deconvblind.html (accessed May 04, 2022).

[17] O. Ronneberger, P. Fischer, and T. Brox, “U-Net: Convolutional Networks for Biomedical Image Segmentation,” in Medical Image Computing and Computer-Assisted Intervention – MICCAI 2015, vol. 9351, N. Navab, J. Hornegger, W. M. Wells, and A. F. Frangi, Eds. Cham: Springer International Publishing, 2015, pp. 234–241. doi: 10.1007/978-3-319-24574-4_28.

[18] I. J. Goodfellow et al., “Generative Adversarial Networks,” arXiv:1406.2661 [cs, stat], Jun. 2014 [Online]. Available: http://arxiv.org/abs/1406.2661

[19] R. J. Noll, “Zernike polynomials and atmospheric turbulence*,” J. Opt. Soc. Am., vol. 66, no. 3, p. 207, Mar. 1976, doi: 10.1364/JOSA.66.000207.

[20] S. Littlefair, “L10: Adaptive Optics.” [Online]. Available: http://slittlefair.staff.shef.ac.uk/teaching/phy217/lectures/telescopes/L10/index.html

[21] J. H. Zhang, “Compensation Through Prediction For Atmospheric Turbulence Effects On Target Imaging and High Energy Laser Beam,” M.S. thesis, Dept. of Mech. and Aero. Eng., NPS, Monterey, CA, USA, 2021 [Online]. Available: http://hdl.handle.net/10945/67840

[22] MATLAB, “Deblurring Images Using the Blind Deconvolution Algorithm,” [Online]. Available: https://www.mathworks.com/help/images/deblurring-images-using-the-blind-deconvolution-algorithm.html

[23] MATLAB, “Create U-Net layers for semantic segmentation,” [Online]. Available: https://www.mathworks.com/help/vision/ref/unetlayers.html

[24] Z. Wang, E. P. Simoncelli, and A. C. Bovik, “Multi-Scale Structural Similarity for Image Quality Assessment,” in 2003 Proc. IEEE Asilomar Conf. on Signals, Systems, and Computers, 2003 [Online]. Availabe: https://ieeexplore.ieee.org/document/1292216

[25] “Peak Signal-to-Noise Ratio as an Image Quality Metric.” National Instruments Corp., Austin, TX, USA, 2020 [Online]. Available: https://www.ni.com/en-us/innovations/white-papers/11/peak-signal-to-noise-ratio-as-an-image-quality-metric.html

[26] MATLAB, “Peak signal-to-noise ratio (PSNR),” [Online]. Available: https://www.mathworks.com/help/images/ref/psnr.html?s_tid=doc_ta

[27] MATLAB, “Structural similarity (SSIM) index for measuring image quality,” [Online]. Available: https://www.mathworks.com/help/images/ref/ssim.html#namevaluepairarguments

THIS PAGE INTENTIONALLY LEFT BLANK

INITIAL DISTRIBUTION LIST

1. Defense Technical Information Center
   Ft. Belvoir, Virginia

2. Dudley Knox Library
   Naval Postgraduate School
   Monterey, California